Geochimica et Cosmochimica Acta xxx (xxxx) xxx

Contents lists available at ScienceDirect

Geochimica et Cosmochimica Acta

journal homepage: www.elsevier.com/locate/gca

Origin of heavy rare earth element enrichment in carbonatites

Wenlei Song [a], Cheng Xu [b,c,*], Martin P. Smith [d], Jindrich Kynicky [e], Jinkun Yang [a], Taotao Liu [a], Delong Jing [f]

[a] State Key Laboratory of Continental Dynamics, Department of Geology, Northwest University, Xi'an 710069, China
[b] Laboratory of Orogenic Belts and Crustal Evolution, School of Earth and Space Sciences, Peking University, Beijing 100871, China
[c] Collaborative Innovation Center for Exploration of Nonferrous Metal Deposits and Efficient Utilization of Resources by the Province and Ministry, College of Earth Sciences, Guilin University of Technology, Guilin 540001, China
[d] School of of Applied Sciences, University of Brighton, Brighton BN24GJ, UK
[e] BIC Brno, Technology Innovation Transfer Chamber, Brno 61200, Czech Republic
[f] MNR Key Laboratory for the Study of Focused Magmatism and Giant Ore Deposits, Xi'an Center of Geological Survey, Xi'an 710054, China

ARTICLE INFO

Associate editor: Adam Simon

Keywords:
Carbonatite
Xenotime
HREE origin
Fractional crystallization
Alkali components
REE deposit

ABSTRACT

Heavy rare earth elements (HREE) are currently in high demand for use in high technology, renewable energy and low-carbon transport, but they are the least abundant in nature. Carbonatites are the primary source of REE; however, they are dominated by light REE (LREE). It remains unknown whether carbonatites have the potential to form economic HREE mineralization. Here we report a xenotime-bearing carbonatite in the Bachu REE deposit, northwestern Tarim Large Igneous Province (TLIP), China, and infer the origin of HREE in carbonatites. The rocks evolved from dolomite to calcite carbonatites, and their HREE content correspondingly increased. Both types of rocks have similar monazite U-Pb ages (ca. 300 Ma), and are older than the major eruption of flood basalt of the TLIP, and associated alkaline complexes. They contain higher $\varepsilon Nd_{(t)}$ (2.4–4.1) and lower initial Sr isotopic ratios [$(^{87}Sr/^{86}Sr)_i = 0.7036–0.7041$] than the basalts but similar values to those of younger alkaline rocks. The carbonatites are inferred to be directly derived from low-degree melting of lithospheric mantle sources induced by a deep-seated mantle plume. Calcite carbonatites contain characteristic xenotime, which is associated with burbankite, sulfates, and minor quartz. The rock-forming calcite shows high HREE abundance and flat REE patterns (La/Ybcn = 0.3–2.1). Apatite and LREE minerals in calcite carbonatites also have a higher HREE content (e.g., Y_2O_3 up to 2 wt%) than those in dolomite rocks. This finding indicates that the early dolomite carbonatite underwent strong fractionation of dolomite and LREE minerals, resulting in HREE and alkali enrichment in the evolved calcite rocks. High amounts of alkalis further enhance the solubility of REE, particularly HREE, in the residual melts. Silica assimilation from the country rocks facilitates the HREE mineralization by sequestering alkalis. Therefore, HREE enrichment in carbonatites may require substantial fractional crystallization of initial melts as well as alkali conservation during ascent.

1. Introduction

Rare earth elements (REE) are critical materials that have received strong attention worldwide in recent years due to their increased importance in new "low-carbon" and "zero-emission" energy technologies and national security applications. For example, the high-strength permanent magnets of emerging electric vehicles and wind turbines heavily rely on REE (Wall et al., 2017). Heavy REE (HREE: Gd-Lu + Y) are notably more valuable than light REE (LREE: La-Sm) in terms of economic significance and predicted high risk of supply shortages (Wall et al., 2017; Goodenough et al., 2017). Currently, HREE are dominantly exploited from granite-related HREE-enriched residual clays in South China (Xu et al., 2017). Carbonatite is a carbonate-rich (usually > 50% in volume) rock, and represents the crystallization products of melts which ultimately derive from the mantle. It contains incredibly high concentrations of LREE resources (typically hosted by monazite and LREE fluorcarbonates). The rock is characterized by high negative-slope chondrite-normalized REE patterns. The enrichment of HREE in carbonatites is uncommon, and only three cases have been reported to contain minor xenotime (e.g., Lofdal, Namibia; Huanglongpu-Huayangchuan,

* Corresponding author at: Laboratory of Orogenic Belts and Crustal Evolution, School of Earth and Space Sciences, Peking University, Beijing 100871, China.
E-mail address: xucheng1999@pku.edu.cn (C. Xu).

https://doi.org/10.1016/j.gca.2023.08.025
Received 14 April 2023; Accepted 28 August 2023
Available online 30 August 2023

China; Songwe, Malawi) (Wall et al., 2008; Song et al., 2016; Broom-Fendley et al., 2017; Smith et al., 2018). The high value of HREE makes the HREE-bearing carbonatites particularly attractive for potential HREE exploitation in the future (Goodenough et al., 2017).

Much previous work has considered that hydrothermal fluids can mobilize REE and concentrate them into economic concentrations (e.g., Migdisov et al., 2016). Most REE mineralization in reported carbonatites, such as the world's largest REE deposit at Bayan Obo, China, is inferred to be of hydrothermal origins (Song et al., 2018; Wei et al., 2022). The HREE in reported carbonatites are also present in late hydrothermal xenotime or fluorapatite (Wall et al., 2008; Broom-Fendley et al., 2017; Bodeving et al., 2017), occurring inside or away from the rocks. Thermodynamic experiments and simulations show that hydrothermal fractionation of HREE from LREE is due to differences in their mobility with transporting ligands (i.e., chloride, hydroxyl-carbonate, and sulfate) at different temperatures (Williams-Jones et al., 2000; Migdisov et al., 2016; Louvel et al., 2022), i.e., hydrothermal mobilization of LREE at T > 400 °C and HREE at T < 200 °C. However, the generation of economic HREE levels at low-temperature hydrothermal systems remains scarce, and significant hydrothermal HREE mineralization may require a magmatic source that is already HREE-enriched. Heavy REE mineral formation in carbonatites has been inferred to be related to post-magmatic hydrothermal fluid-induced dissolution-reprecipitation of preexisting HREE-bearing minerals (e.g., carbonates, apatite, and zircon) (Wall et al., 2008; Bodeving et al., 2017; Smith et al., 2018). This condition indicates that the initial concentration of HREE during the magmatic stage is pivotal for REE redistribution. The importance of magmatic processes in the concentration and fractionation of REE has been experimentally constrained in recent years (Anenburg et al., 2020; Nabyl et al., 2020; Mollé et al., 2021; Nikolenko et al., 2022). However, many experiments focus on forming LREE and Nb minerals, such as britholite, pyrochlore, and burbankite. The origin of HREE minerals (i.e., xenotime) in the carbonatitic magmas is still poorly constrained. Here, we report a xenotime-bearing carbonatite in the Bachu area, China. The rocks consist of dolomite and calcite carbonatites and show different levels of LREE and HREE enrichment. They retain primary LREE and HREE mineral assemblages and are valuable natural laboratories for understanding HREE origin, fractionation, and deposition during carbonatite magma evolution.

2. Geological settings

The Bachu carbonatite REE deposit is located in the northwestern part of Tarim Large Igneous Province (TLIP; Supplementary Fig. S1A, Tian et al., 2010; Zhang et al., 2013; Xu et al., 2014). The Tarim Block is surrounded by the Tianshan Mountains in the north and west and the western Kunlun and Altyn orogenic belts in the south. Based on geophysical and oil exploration deep-drilling, the TLIP covers an area of >300,000 km^2, with a thickness of igneous package ranging from several hundred meters to three kilometers (Tian et al., 2010; Xu et al., 2014). Magmatism related to plume activities at different timings is present within the region (Zhang et al., 2008, 2013; Xu et al., 2014): (1) ~300 Ma small-volume kimberlite, representing the onset of a plume-induced event; (2) ~290 Ma flood basalt and rhyolite, which produced the bulk of igneous rocks at Tarim; and (3) emplacement of small-volume ~270 Ma mafic–ultramafic dikes, syenites, and A-type granites at ~280 Ma contemporaneous with another episode of rhyolitic volcanism (282–277 Ma).

The REE deposit is located ~40 km southeast of Bachu town and occurs within the Wajilitage layered mafic–ultramafic complex (Fig. S1B). The complex is 5 km in length and 1.5–3 km in width, occupying an area of ~12 km^2, and is dominantly composed of pyroxenite, clinopyroxenite, and gabbro (Zhang et al., 2008; Cheng et al., 2017). The REE carbonatites occur as a swarm of NWW-SEE trending dikes over ca. 5 km^2 (Fig. S1B) and are distributed in the northern part of the complex. They intrude pyroxenite, gabbro, and Devonian clastic sequences and have an enormous output scale with lengths ranging from 200 m to >1000 m and thicknesses up to 15 m (Cheng et al., 2017). In addition, some of the wall rocks are fenitized due to alkali metasomatism. These dikes dip at 70–80° and can be tracked to depths of at least 1000 m (Cheng et al., 2018). They are composed of dolomite and calcite carbonatites, and both developed REE mineralization. The carbonatites usually show inhomogeneous and remarkably variable mineral abundances and associations from the scale of hand specimen to the whole rock body. Monazites separated from a calcite-dominant rock gave a Th-Pb age of 266 ± 5 Ma (Song et al., 2017). Some LREE-rich (total REE_2O_3 up to 20 wt%), red veins consisting of barite, celestine, apatite, and monazite occur within the dolomite carbonatites (Cheng et al., 2018). According to the report by the Geological Team No. 11 of the Xinjiang Geological Bureau, 24 carbonatite orebodies have been recognized in outcrops and drill cores. The estimated REE_2O_3 grade of the deposit is between 0.54 and 1.92 wt%, with total REE_2O_3 resources of beyond 300 kilotons.

3. Analytical methods

Measurements of the mineral composition and texture in the carbonatites were carried out using a high-resolution Zeiss scanning electron microscope (SEM) with an attached Oxford INCA-ENERGY 300 X-ray spectrometer (EDS) at Peking University, China. The samples were coated with a conductive carbon layer and analyzed in High Vacuum Mode at typical working conditions of accelerating voltage 15 or 25 kV and a working distance of 15 mm.

Major-element compositions of representative minerals were determined by wavelength-dispersive X-ray spectrometry using a Cameca SX100 electron microprobe at Masaryk University, Czech Republic. The microprobe was operated at an accelerating voltage of 15 kV and a beam current of 20 nA, with an electron beam defocused to a 5–10 μm spot to limit devolatilization ionic diffusion and other forms of beam damage in the samples. The following major standards and X-ray emission lines were used in the analysis: albite (Na, Kα), sanidine (Si, Kα), celestine (Sr and S with Lα and Kα, respectively), fluorapatite (P and Ca both with Kα), baryte (S and Ba with Kα and Lα, respectively), topaz (F, Kα), synthetic ThO_2 (Th, Mα) and U (U, Mb). For REE, synthetic REE glasses and orthophosphates (La, Ce, Sm, and Y with Lα lines; Pr, Nd, Gd, and Dy with Lβ lines) were used. The data were reduced and corrected using the PAP routine (Pouchou and Pichoir, 1984).

Major and trace element analyses of the whole-rock powders were conducted by inductively coupled plasma optical emission spectrometry (ICP-OES, PE 8300V) and mass spectrometry (ICP-MS, Agilent 7700E) at the Xi'an Zhaonian Mineral Testing Technology Co., Ltd., China. The fresh whole-rock samples were crushed using a tungsten carbide ball mill and then 200 mesh sieved. Before analyses, sieved samples were decomposed and dissolved using a three-acid mixture of 10 ml HF, $HClO_4$, and HNO_3 (2:1:1) in high-pressure Teflon containers at 190 °C at least 48 h. This was followed by two cycles of dilution and evaporation to dryness. Next, the dry residue was re-dissolved in 5 ml of aqua regia to exact and cool. The final solution was diluted to 50 ml by adding distilled de-ionized water for analysis. Major and trace element analyses were carried out using the ICP-OES and ICP-MS, respectively. ^{103}Rh and ^{185}Re (10 ppb mixing) were used as the internal standard for trace elements. The analytical precision is generally better than 5% and 10% for most major and trace elements, respectively.

In-situ laser-ablation (LA)-ICP-MS trace element analyses of the calcites, dolomites, and apatites were performed at Peking University, China. The instrument consists of COMPexPro102 Excimer Laser and Agilent7500ce/cs type ICP-MS. The diameter of the ablation spot used was 32 μm. NIST 610 glass was used as a calibration standard for all samples. The element used for the internal standard was P_2O_5 for apatite and CaO for carbonates, respectively, which were independently measured by the electron microprobe mentioned above. In-run signal intensity for indicative trace elements (e.g., Sr, La, Ce, et al.) was

monitored during analysis to ensure that the ablation spot was confined to the area of interest and did not sample other mineral phases or inclusions. The analytical precision of the measurements is better than 5% at the ppm level.

The U-Th-Pb isotopic monazite dating was obtained by LA-ICP-MS at Xi'an Geological Survey Center, China Geological Survey. Spot analyses were conducted on thin sections using a laser beam with a 36 μm spot size, an energy density of 6 J/cm^2, and an ablation rate of 6 Hz. Helium was chosen as the carrier gas, and the gas flow rate was sustained at 550 ml/min. The acquisition times for background and samples were 40 s and 30 s, respectively. Monazite standard 44069 and glass NIST610 were used as external standards for U-Th-Pb dating and trace element calibration, respectively. These standards were analyzed at the initiation and end of a series of measurements. In addition, the Excel-based software ICPMSDataCal was used to perform offline selection and integration of background and analyzed signals, time-drift correction, and quantitative calibration for trace element analysis and U-Th-Pb dating.

The in-situ Sr isotopic compositions of the Sr-bearing minerals (apatite, calcite, dolomite, baryte, celestine, and strontianite) were analyzed by LA-MC-ICP-MS (GeoLas 2005 + Neptune Plus) at China University of Geosciences (Wuhan). Isotopes were acquired in static multi-collector mode with low resolution using seven Faraday collectors and the mass configuration array from ^{82}Kr to ^{88}Sr to monitor Kr, Rb, and Sr. More detailed analytical procedures and data reduction strategies were described by Tong et al. (2015).

In-situ Nd isotopic analysis of monazite grains was done by LA-MC-ICPMS using a Thermo-Finnigan Neptune instrument coupled to a 193 nm ArF Excimer laser-ablation system at the Institute of Geology and Geophysics, Chinese Academy of Sciences. The laser was focused at 24 μm above the sample surface and fired using a 6 Hz repetition rate and an energy density of 10 J/cm^2. An in-house apatite standard (AP1) and Jefferson monazite 44069 were used for external calibration. Normalized ^{143}Nd/^{144}Nd and ^{147}Sm/^{144}Nd isotopic ratios were calculated using the exponential law. During the analytical sessions, the ^{147}Sm/^{144}Nd ratio was externally calibrated against the ^{147}Sm/^{144}Nd ratio of standard reference materials. Detailed analytical procedures have been described by Yang et al. (2008).

4. Results

4.1. LREE and HREE mineralogy

Field observations show that calcite carbonatite crystallization followed that of dolomite carbonatites (Cheng et al., 2018). The latter consists of large euhedral coarse-grained dolomite with crystals (>90 vol%) measuring up to 2 mm in diameter and showed triple-junction

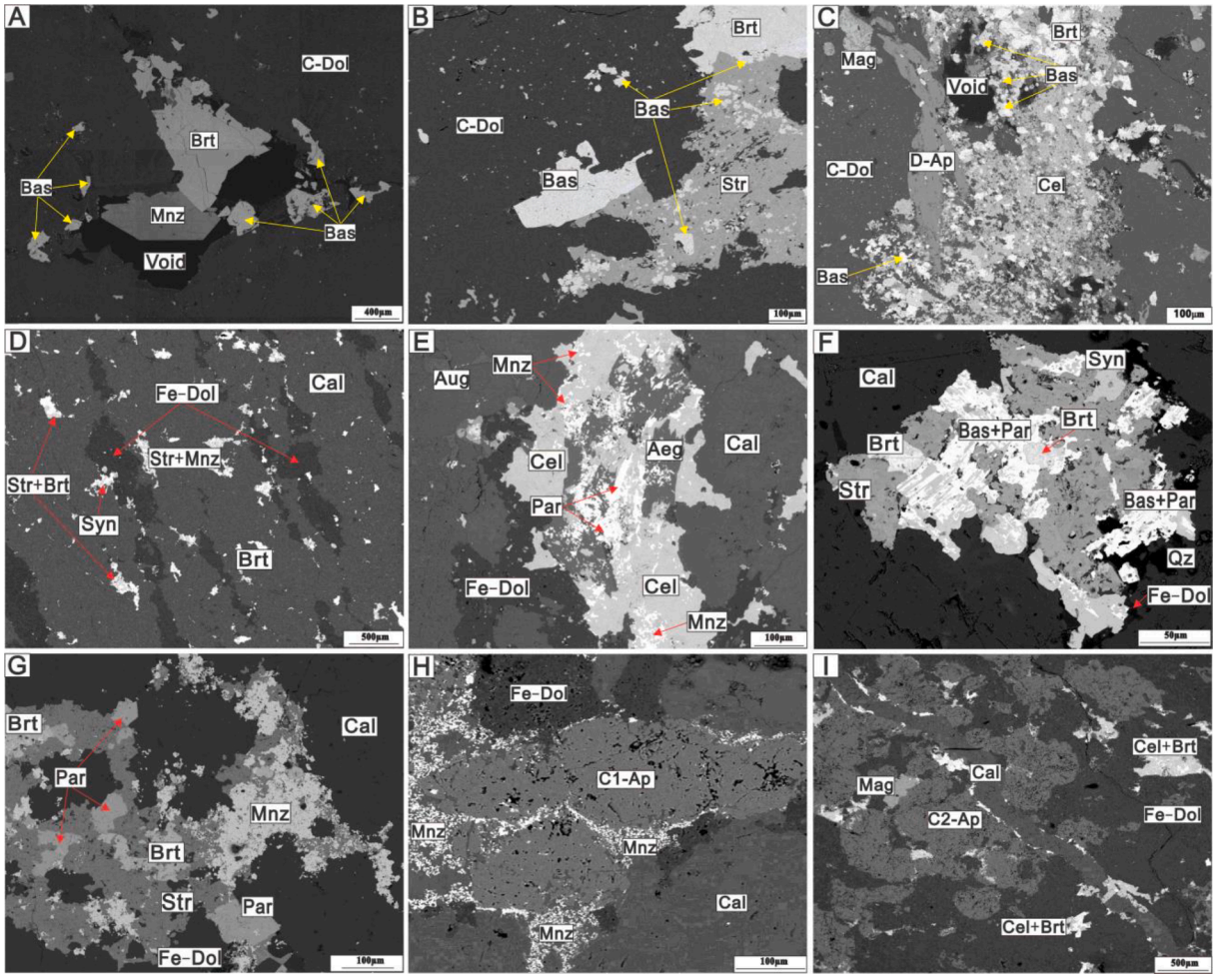

Fig. 1. Representative backscattered electron microscopic images of LREE mineralization in dolomite (A–C) and calcite (D–I) carbonatites. (A–C) Monazite, bastnäsite, and apatite associated with baryte, celestine, and strontianite form relatively large crystals and filled the voids of the coarse-grained dolomite matrix; (D–E) LREE minerals occur as ferrodolomite-dominated veinlets penetrating the calcites; (F–G) LREE mineral intergrowth with ferrodolomite, sulfates, strontianite, and quartz occur within the calcite matrix; (H) monazite is present as tiny polycrystalline aggregates along the rim of apatite; (I) hydrothermal calcite-sulfate veinlet cross-cutting calcite carbonatites. Aeg, aegirine; Ap, apatite; Aug, augite; Bas, bastnäsite; Brt, baryte; Cel, celestine; Cal, calcite; C-Dol, coarse-grained dolomite; Fe-Dol, ferrodolomite; Mag, magnetite; Mnz, monazite; Par, parisite; Qz, quartz; Str, strontianite; Syn, synchysite.

grain boundaries (Fig. S2A). Fine- to medium-grained calcite (>85 vol %) makes up calcite carbonatites (Fig. S2B–D), which contain >10 vol% dolomite and ankerite, different to the reported calcite-dominant carbonatites in Song et al. (2017). Dolomite carbonatite experienced subsolidus hydrothermal superposition and formed a patched LREE mineralization overprinting on the dolomite grains (Fig. 1A–C). The REE-rich minerals of monazite, bastnäsite, and apatite occur as disseminations and veinlets associated with strontianite, baryte, and celestine. In calcite carbonatite, the LREE-rich minerals are composed of monazite, bastnäsite, parisite, synchysite, and apatite. They mainly occur as veinlets (Figs. 1D, E, G, and S2C) and patched (Figs. 1F and S2D) assemblages intergrown with ferrodolomite, baryte, and strontianite. Minor aegirine and quartz are associated with the REE minerals. Monazite is also present as tiny polycrystalline aggregates along the rim of apatite (Fig. 1H). The calcite-sulfate veinlets cross-cut the apatite and ferrodolomite assemblages in calcite carbonatites (Fig. 1I), representing a late hydrothermal event. However, no REE mineralization is associated with late veinlets. Fluorite, which is present in many carbonatite-hosted REE deposits (e.g., Mountain Pass, USA, Watts et al., 2022; Bayan Obo and Mianning-Dechang belt, China; Xu et al., 2012), was not observed in the samples.

In addition to LREE minerals, many xenotime grains have been found in calcite carbonatite (Fig. 2). They generally intergrow with monazite and sulfates. There are four types of occurrences observed: (1) patched association with burbankite and baryte (Fig. 2A–D); (2) occasional veinlets and patched clustering with sulfates (Fig. 2E, F); (3) intergrowth with quartz, aegirine, and/or albite and replacement and overgrowth along with apatite (Fig. 2G); and (4) dissemination in ferrodolomite-dominated veinlets that infiltrated calcite (Fig. 2H, I). The HREE minerals were not found in the late calcite-dominant carbonatites (Song et al., 2017).

4.2. Mineral chemistry

Supplementary Tables S1 and S2 list the major and trace element compositions of carbonate, apatite, rare earth and silicate minerals from the carbonatites, respectively.

4.2.1. Carbonates

In this study, five types of carbonate minerals can be distinguished in the carbonatites based on their textures and compositions (Fig. 3): (1) Rock-forming, coarse-grained magmatic dolomite in dolomite carbonatites (C-Dol; Figs. 1A–C and S3A). The mineral contains high amounts of SrO (1–1.5 wt%) and MnO (0.8–1 wt%) with relatively constant MgO (~20 wt%), CaO (~30 wt%), and FeO (~2 wt%) contents. (2) Hydrothermal dolomite (Fe-Dol; Figs. 1 and 2). It occurs as a veinlet associated with LREE and HREE minerals within calcite carbonatites. The mineral is ferrodolomite in composition with variable FeO contents (4–10 wt%). Its MgO and FeO compositions display a negative linear relationship. The hydrothermal dolomite shows a relatively lower SrO (mostly < 1 wt %) but higher MnO (1–1.5 wt%) than the above rock-forming dolomite. (3) Rock-forming, coarse-grained magmatic calcite in calcite

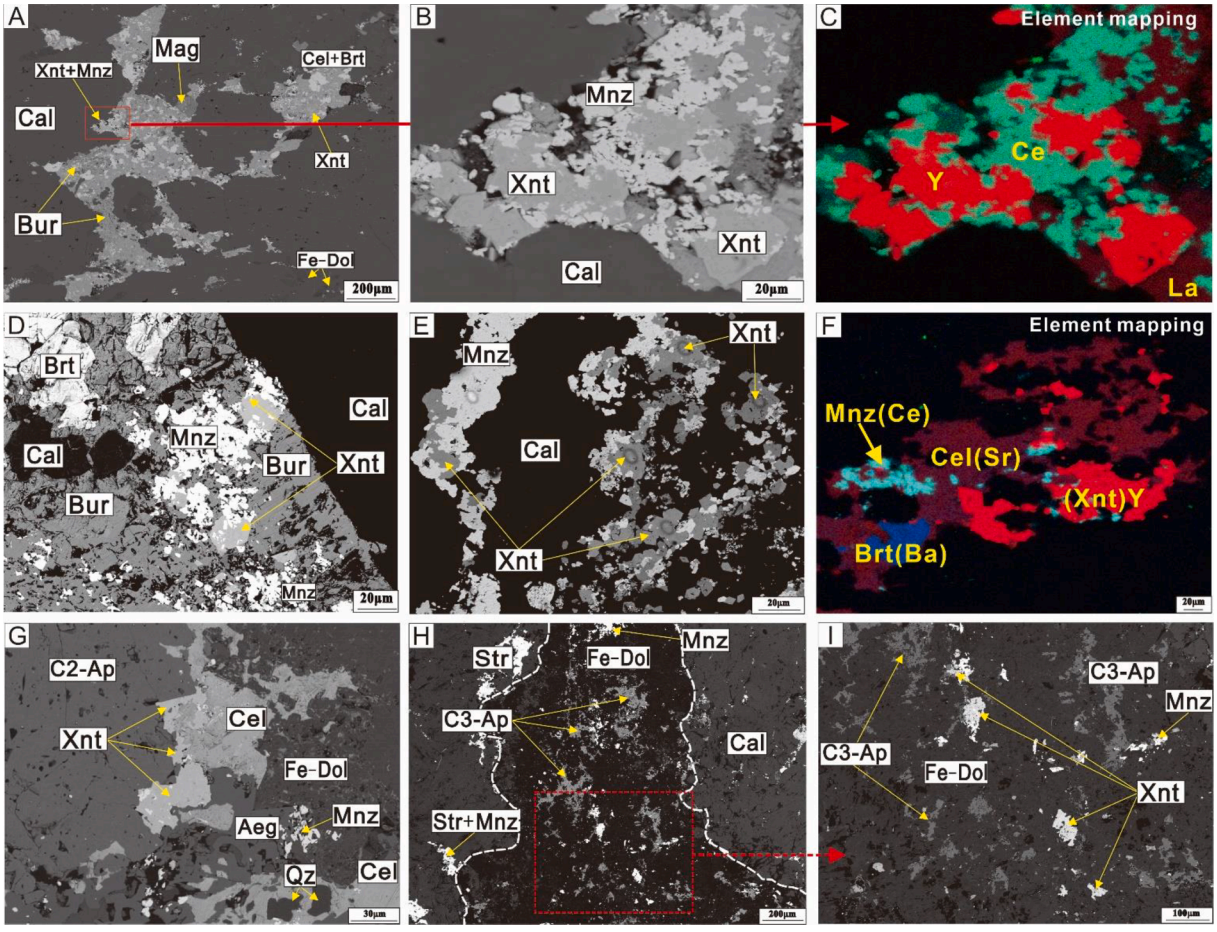

Fig. 2. Representative backscattered electron images of xenotime in calcite carbonatite. (A–D) Xenotime intergrowth with monazite, burbankite, and sulfates occurs as patched, or veinlet clusters; (E–F) xenotime intergrowth with monazite and sulfates forms disseminated euhedral small aggregates; (G) xenotime associated with monazite, quartz, and aegirine partially replaces apatite, forming a thick overgrowth along apatite; (H–I) xenotime occurs within ferrodolomite-dominated veinlet. Aeg, aegirine; Ap, apatite; Brt, baryte; Bur, burbankite; Cal, calcite; Cel, celestine; Fe-Dol, ferrodolomite; Mag, magnetite; Mnz, monazite; Qz, quartz; Str, strontianite; Xnt, xenotime.

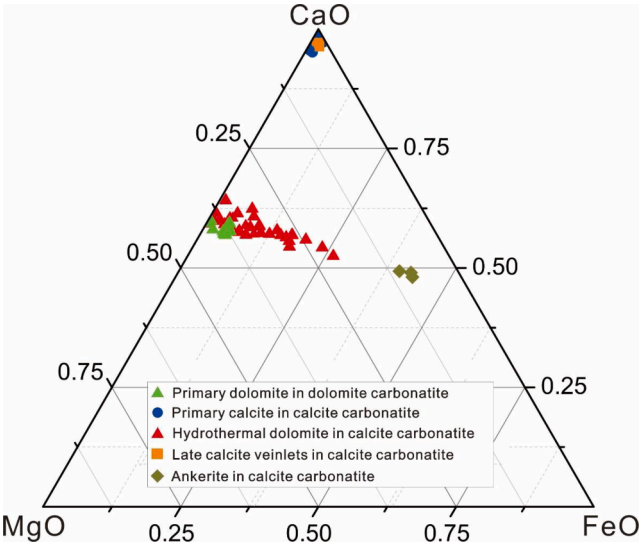

Fig. 3. CaO–MgO–FeO ternary plots for carbonates from Bachu carbonatite.

carbonatites (Figs. 1, 2, and S3B). This mineral has the near end-member composition of carbonate mineral with minor concentrations of SrO (0.2–0.6 wt%), FeO (0.2–0.7 wt%), and MgO (0.1–0.2 wt%). (4) Late hydrothermal REE-barren calcite-sulfate veinlets cross-cutting calcite carbonatites (Fig. 1I). They probably represent the final stage and residual fluids of carbonatite evolution. Calcite shows higher MgO (1–1.3 wt%) and SrO (0.7–1 wt%) abundances than the primary phase. (5) Sparse ankerite. They contain high amounts of FeO (22–25 wt%) and are present in the hydrothermal REE mineralization assemblage within the calcite carbonatites.

All the carbonate minerals show positive Ba, Th, and Sr and negative Nb, Ta, Zr, and Hf anomalies relative to the primary mantle values (Fig. 4A), similar to most carbonates from carbonatites worldwide (Woolley and Kempe, 1989; Hornig-Kjarsgaard, 1998). The primary dolomite is characterized by markedly lower U, Nb, and Ta concentrations than the magmatic calcite. Hydrothermal calcite and dolomite in the calcite carbonatites show variable Pb compositions from negative to positive anomalies. The former generally has the highest Ba, Th, Sr, and LREE abundances among the carbonates. In chondrite-normalized REE diagrams (Fig. 5A), the primary dolomite and calcite exhibit different distribution patterns. The former has a low REE content and shows LREE enrichment relative to HREE (La/Ybcn = 27–73). Magmatic calcite is characterized by a relatively flat REE pattern with La/Ybcn = 0.33–2.1, different from the previously identified characteristic LREE-enriched feature of carbonatitic calcite (Hornig-Kjarsgaard, 1998). Moreover, it presents a high HREE composition. In contrast, hydrothermal calcite in the veinlets shows a strong LREE enrichment (La/Ybcn = 7–136). Low REE abundance and a relatively flat pattern (La/Ybcn = 0.35–3.69) were observed in the hydrothermal dolomite. Calcite and dolomite have no Ce (Ce/Ce* ~ 1.1) and Eu (Eu/Eu* ~ 1) anomalies.

4.2.2. Apatite

Based on mineral association and textures, we recognized one type (D) and three types (C1, C2, and C3) of apatites in the dolomite and calcite carbonatites, respectively (Figs. 1 and 2). Type D, C1, and C2 apatites usually form large euhedral to subhedral crystals within the rock-forming carbonate matrix, indicating a magmatic origin. The C1-apatite is rare and occurs as disseminated grains overgrown by small monazite aggregates (Fig. 1H), implying fluid-induced metasomatism. The C2-apatite is much larger and more abundant and generally present as clustered assemblages. The C3-apatite is of hydrothermal origin and occurs within ferrodolomite-dominated veinlets, intruding into the calcite carbonatites (Fig. 2H, I). All apatites belong to fluorapatite (F = 1.8–5.9 wt%) and have variable REE compositions (total REO: 0.3–7.8 wt%). Their P_2O_5 contents (~39 wt%) are relatively constant, and the CaO contents negatively correlate with the total REO compositions (Fig. S4). The observed D apatite generally has a lower F (1.8–2.8 wt%) and higher SrO (3.2–4.8 wt%) than the three types of apatites (F: 1.8–5.9 wt% and SrO: 0.7–1.7 wt%) in the calcite carbonatite. The former has low Y_2O_3 contents below the detection limit of the EPMA. In contrast, apatite in the calcite carbonatite has detectable Y_2O_3 abundances ranging from 0.2 wt% to 1.4 wt%.

The different types of apatites show variable trace element compositions. Type D apatite exhibits negative Pb, Sr, Zr, and Hf anomalies. It has higher amounts of Sr and LREEs, but lower U, Nb, Ta, Zr, Hf, and HREE contents relative to the minerals in calcite carbonatites (Fig. 4B). Type C1 and C3 apatites are characterized by negative Pb and Sr anomalies, different from Type C2. Higher trace element (except Sr) concentrations were determined in Type C1. The chondrite-normalized REE patterns (Fig. 5B) for Type D apatite are characterized by the most significant LREE enrichment and LREE/HREE fractionation with a higher La/Ybcn ratio (953–4383) compared with the C1–C3 apatites. The former contains the lowest HREE concentrations. In contrast, Type C1 has the highest HREE contents and shows LREE enrichment with a La/Ybcn ratio of 11–52; Type C2 contains the lowest total REE abundance, and an intermediate total REE content was determined in Type C3. Types C2 and C3 display slight LREE enrichment (La/Ybcn = 2.2–9.4 and 1.7–4.4, respectively) and convex REE patterns with a La/Ndcn<1. The four types of apatites show a positive relationship between total REE and Si contents (Fig. 6). This finding is consistent with the experimental results, which suggest that high Si activity in carbonatitic melts favor REE incorporation into apatite (Hammouda et al., 2010; Anenburg et al., 2020). A similar linear correlation between Y (HREE) and Si was observed in Types C1–C3. Although the apatite in dolomite carbonatite contains high Si abundance, it has relatively low HREE content. This result indicates that the primary dolomitic melt may be depleted in HREE.

4.2.3. Rare earth minerals

In the carbonatites, all LREE minerals are Ce-dominated varieties. The compositions of different types of monazites from the dolomite and calcite carbonatites systematically vary according to (La + Ce + Pr)/total REO versus La/Ndcn diagram, showing a relatively low LREE ratio (<0.83) and fractionation (La/Ndcn < 5) in the calcite carbonatites (Fig. 7A). Similar to the apatite, monazite in the dolomite carbonatite contains low Y_2O_3 contents (most below the EPMA detection limit) and high LREE fractionation (La/Ndcn > 15). In contrast, monazite Y_2O_3 contents in the calcite carbonatite were determinable (0.3–2 wt%). Bastnäsite in the dolomite carbonatite also shows relatively lower HREE concentrations (Y_2O_3 = 0.04–0.29 vs. 0.31–1.16 wt%) and higher La/Ndcn ratios than that in the calcite carbonatite. Synchysite and parisite are only present in the calcite carbonatites. Both contain detectable Y_2O_3 (0.31–1.11 wt%) and show similar low La/Ndcn values to monazite (Fig. 7B). The major element concentrations of burbankites and xenotimes are relatively constant and independent of their different textures and the minerals they are associated with. The burbankite is Na-, Ca-, Sr-, and LREE dominated and have compositions with an REO of 28.3–32.3 wt%. Xenotime is dominated by Y_2O_3 (41.3–46 wt%) and contains minor Gd, Dy, and Er (averge 2.97, 7.33, 2.95 wt% oxides, respectively).

4.2.4. Silicate minerals

Silicate minerals, such as aegirine, albite, and quartz, were observed in the calcite carbonatites and mostly associated with xenotime (Fig. 2). Aegirine shows no evident variations in the major element contents (Ae_{95-96}). It is dominated by Na_2O (~14 wt%), SiO_2 (~54 wt%), and total iron oxide (~28 wt%), with minor proportions of Al_2O_3, MgO, and CaO (<2 wt%). Albite is homogeneous in composition ($Ab_{99}An_{0.8}Or_{0.2}$) and contains minor amounts of CaO (~0.2 wt%) and FeO (~0.1 wt%).

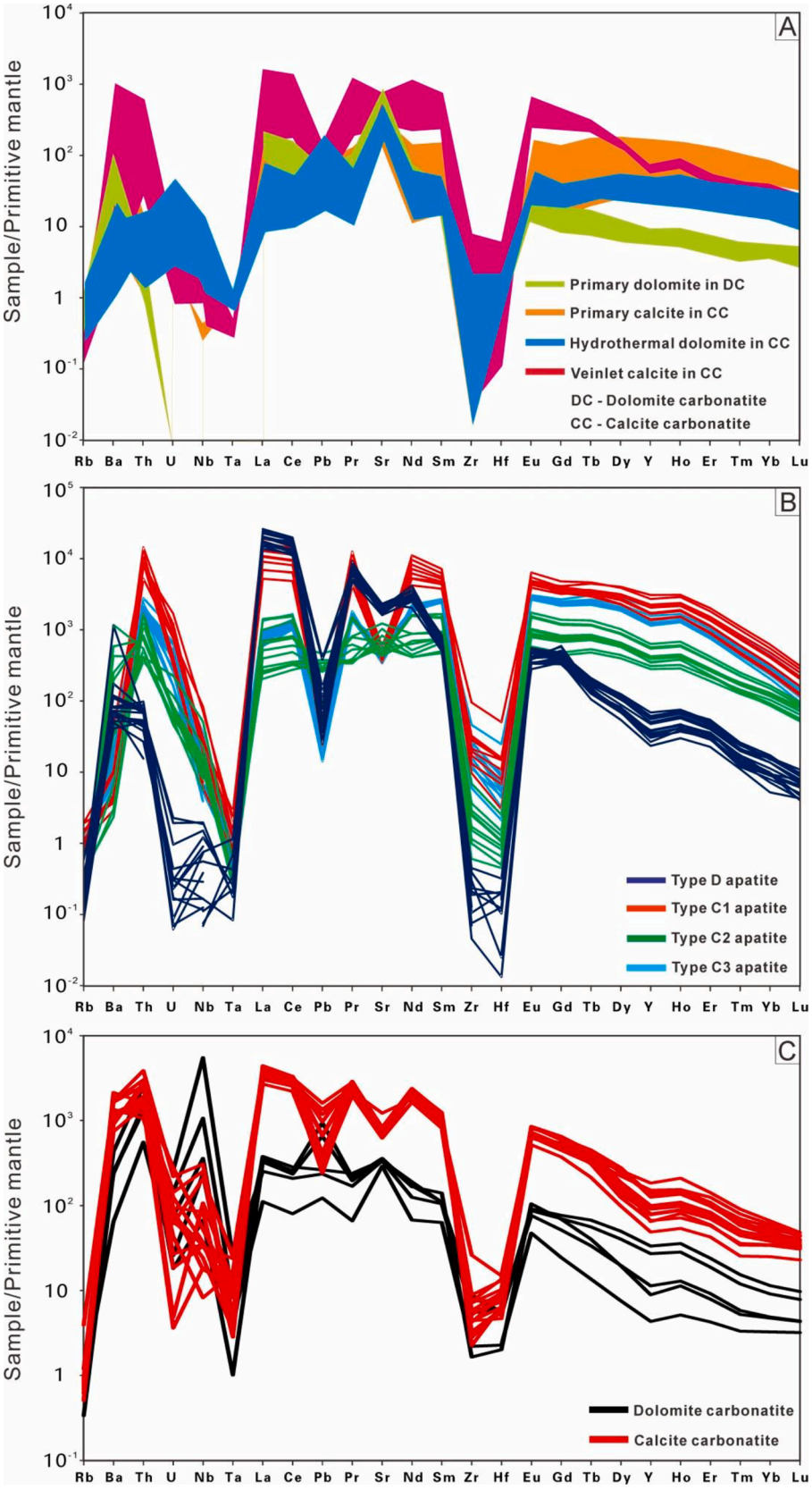

Fig. 4. Primitive mantle-normalized trace element diagrams of carbonates (A), apatites (B), and whole rock (C) of Bachu carbonatites.

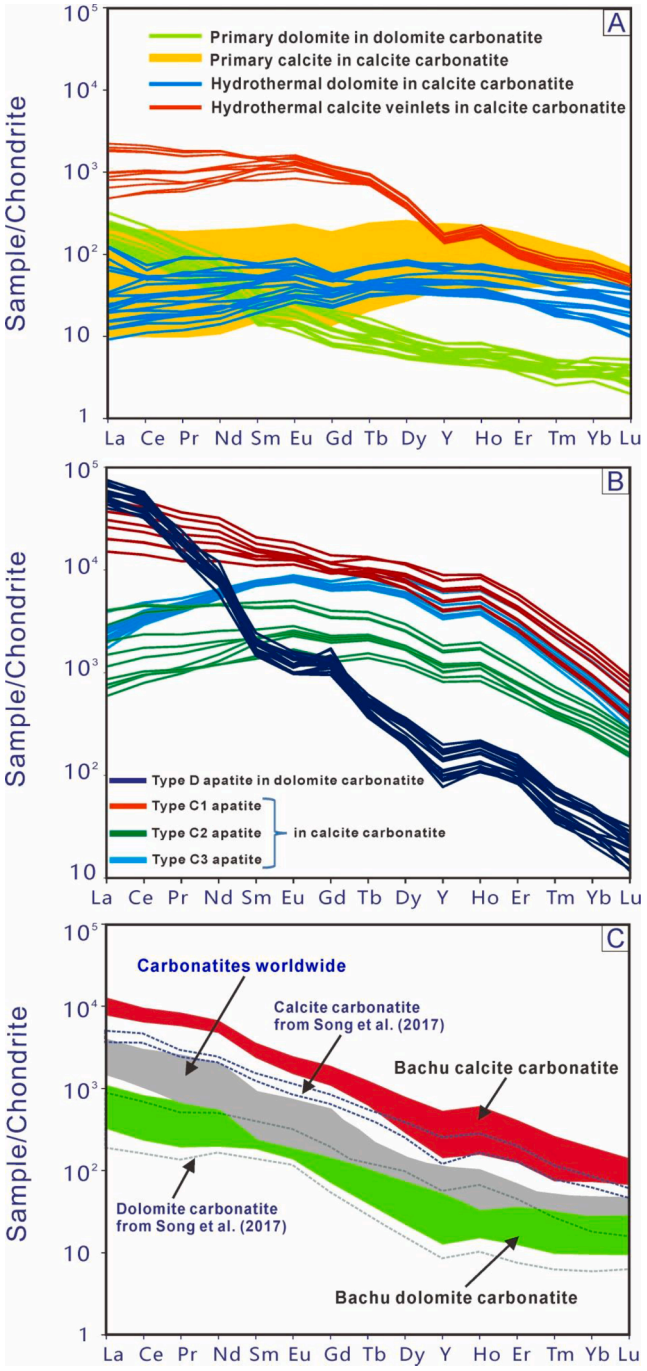

Fig. 5. Chondrite-normalized REE patterns of carbonates (A), apatite (B), and whole rock (C) of Bachu carbonatites. Carbonatites worldwide were from Woolley and Kempe (1989).

4.3. Whole-rock compositions

Table S3 provides the major and trace element compositions of the carbonatite samples. According to the CaO–MgO–FeO_t + MnO composition classification of Woolley and Kempe (1989), the carbonatites mainly correspond to magnesiocarbonatite and calciocarbonatite (Fig. S4). Dolomite carbonatite shows homogeneous compositions with low SiO_2 (≤1.0 wt%) and alkalis ($K_2O + Na_2O \leq 0.2$ wt%) and relatively constant FeO_t (2.5–4.6 wt%) and MgO (17–18.6 wt%) contents. In contrast, the calcite carbonatite exhibits variable SiO_2 (0.2–6.8 wt%), FeO_t (1.5–4.1 wt%), MgO (2.4–6.5 wt%), and P_2O_5 (0.1–8.5 wt%) contents due to the heterogeneous distribution of carbonates (i.e., ferrodolomite), silicates, and apatites with the above mineral compositions (Figs. 1, 2).

Fig. 4C presents the primitive mantle-normalized plots for the whole-rock trace element compositions. Both rock types show overall enrichment in trace elements. The calcite carbonatite exhibits higher trace element concentrations (except U, Nb, and Pb) than the dolomite rocks. The former has more negative Pb and Sr anomalies than dolomite carbonatite. They show consistent LREE enrichment patterns with La/Ybcn = 33–69 and 57–108 for the dolomite and calcite carbonatites, respectively (Fig. 5C). Ce and Eu anomalies were not determined in the rocks. The calcite carbonatite has higher REE concentrations, especially HREE, than the dolomite carbonatites and reported calcite-dominant (MgO < 1 wt%) carbonatite dikes in the deposit (Song et al., 2017), and average carbonatites worldwide (Woolley and Kempe, 1989). This feature is consistent with our mineralogy observations showing the prevalence of HREE-bearing minerals in the calcite carbonatite.

4.4. U–Th–Pb geochronology and Sr–Nd isotopes

Monazite is a typical REE mineral in the two types of carbonatites. This mineral in the dolomite carbonatite has high Th and U concentrations and low Th/U ratios (130–165; Table S4). It yields a low intercept age of 300 ± 8.7 Ma in the Tera–Wasserburg plot (Fig. 8A). The U content of monazite in the calcite carbonatite is extremely low to derive a reliable U–Pb age, whereas the Th content is relatively high. The analyzed grains give a weighted mean Th–Pb age of 301 ± 5.9 Ma (Fig. 8B). Both rocks are older than the HREE mineral absent, calcite-dominant carbonatite dikes (monazite Th-Pb age of 266 ± 5 Ma; Song et al., 2017).

In-situ analyses of Sr isotopic compositions of calcite, dolomite, apatite, strontianite, baryte, and celestine associated with LREE and HREE mineralization show that all these Sr-bearing minerals have limited and nearly identical radiogenic Sr isotopic ratios [$(^{87}Sr/^{86}Sr)_i$ = 0.7036–0.7041] (Fig. 9; Table S5). In-situ Nd isotope compositions of monazites from the dolomite carbonatites reveal slight variations, with $^{143}Nd/^{144}Nd$ ratios ranging from 0.512450 to 0.512566 and corresponding positive $\varepsilon_{Nd(t)}$ values (2.4–4.1). Their Nd isotopic model ages (T_{DM}) range from 0.50 to 0.58 Ga (Table S6). These initial Sr-Nd isotope compositions are similar to those of the dolomite and calcite carbonatites (Cheng et al., 2017), which indicates that HREE originate from the carbonatite without any external material contribution.

5. Discussion

5.1. Origin of carbonatites

Carbonatites worldwide are mostly confined to the continental lithosphere (e.g., rift or orogenic belt) and two localities (Cape Verde and Canary) in the oceanic lithosphere (Woolley and Bailey, 2012; Humphreys-Williams and Zahirovic, 2021). Some carbonatites that have been spatially and temporally associated with large igneous provinces are considered to originate from a deep-mantle plume source (Ernst and Bell, 2010). Similar Sr-Nd-Pb-Hf isotopic compositions between young carbonatites and ocean island basalts demonstrate the involvement of plumes in carbonatite petrogenesis (Simonetti et al., 1998; Bell and Tilton, 2001). However, whether terrestrial carbonatite rocks are derived from lithospheric or asthenospheric mantle sources has been debated in recent decades. The carbonatite lavas in Oldoinyo Lengai, Tanzania, show similar $^3He/^4He$ ratios and overlap with those of samples of mid-ocean ridge basalts (MORB) and lithospheric mantle (Fischer et al., 2009). The repetition of carbonatite magmatic activities within the same area over a long time (e.g., 1 billion years) led Woolley and Bailey (2012) to propose that the lithospheric mantle is the carbonatite source, precluding any direct role of plumes. Our work provides direct geochemical evidence to support that the carbonatite origin is unrelated to plume compositions.

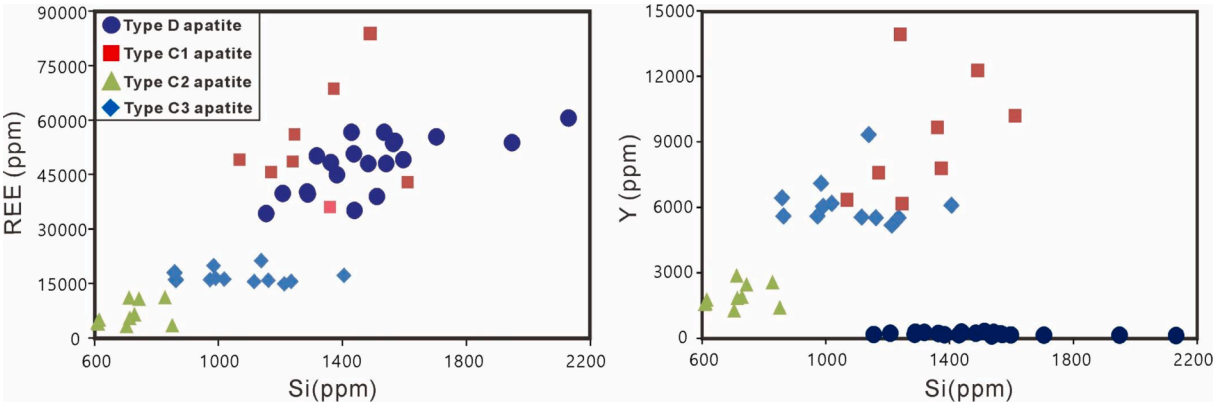

Fig. 6. Plots of total REE, Y vs. Si (ppm) of apatite from Bachu carbonatite.

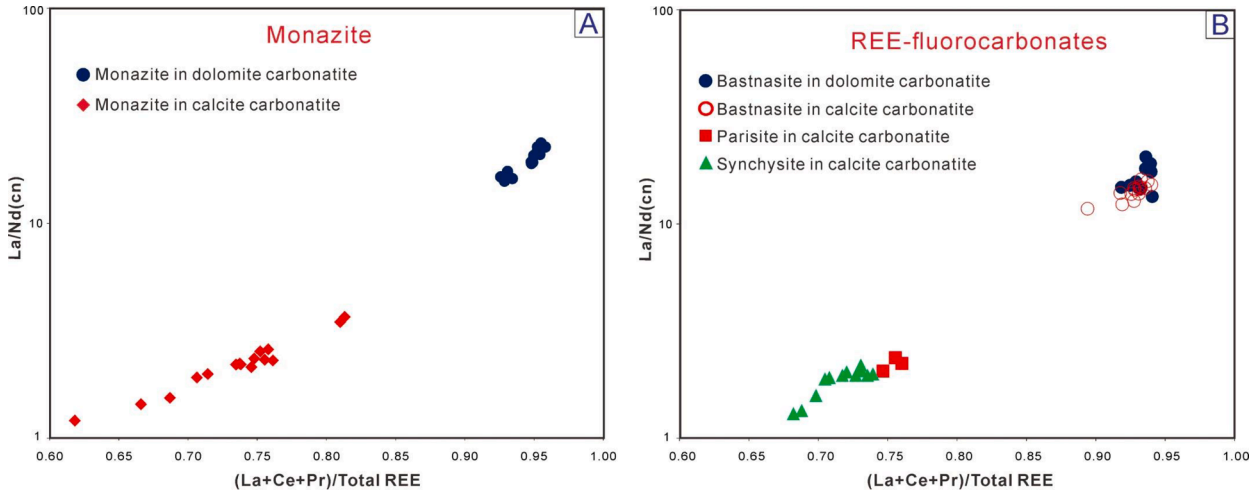

Fig. 7. (La + Ce + Pr)/total REE vs. La/Nd(cn) diagrams of monazite (A) and REE–fluorocarbonates (B) from Bachu carbonatites.

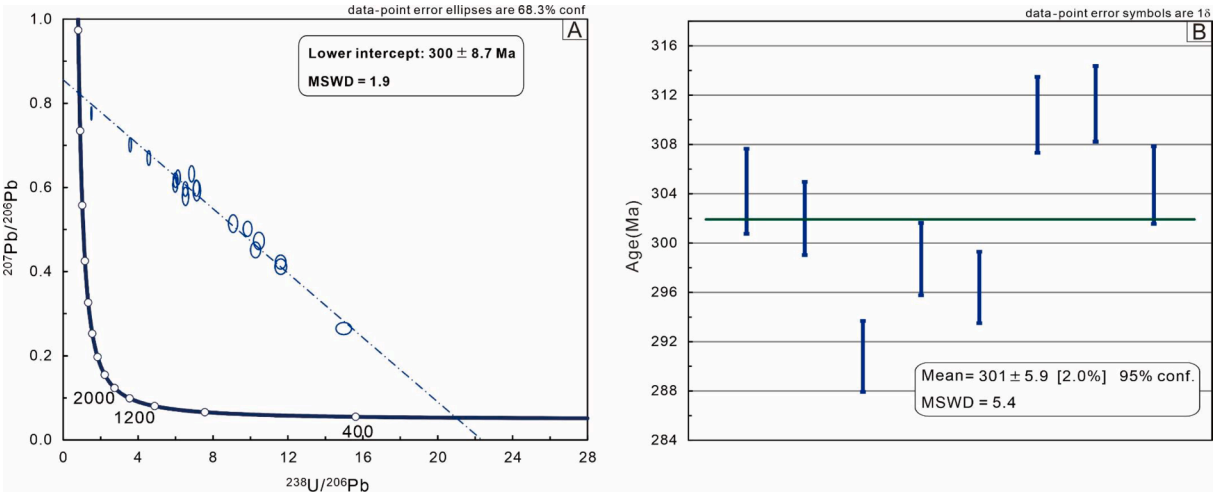

Fig. 8. U–Th–Pb data of monazite from Bachu carbonatites. (A) Tera–Wasserburg concordia plot for U–Pb ages of monazite in dolomite carbonatite; (B) weighted average plot of the $^{208}Pb/^{232}U$ ages of monazite from calcite carbonatites.

The Bachu carbonatite is located in the northwestern part of TLIP (Fig. S1A). Both dolomite and calcite carbonatites (ca. 300 Ma; Fig. 8) were emplaced ~10 Ma earlier than the main eruption age of flood basalt (~290 Ma; Zhang et al., 2008; Xu et al., 2014). A few ~266 Ma carbonatite dikes were also observed in the deposit, forming significantly later than the flood basalt (Song et al., 2017). All the carbonatites are characterized by consistently high εNd and low $^{87}Sr/^{86}Sr$, different from TLIP (Fig. 9). Moreover, late alkali magma activities (~270 Ma) of nephelinite, lamprophyre, and syenite show similar depleted Sr–Nd isotope compositions (Fig. 9). This finding indicates that

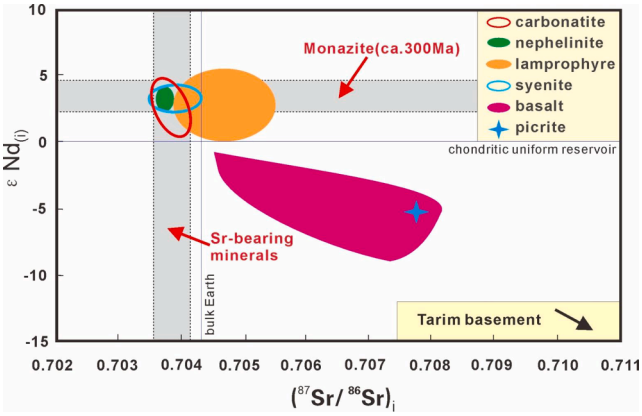

Fig. 9. Variations in $(^{87}Sr/^{86}Sr)_i$ of Sr-bearing minerals and εNd of monazite from Bachu carbonatites compared with the published whole rock and associated igneous rocks. Carbonatite: Cheng et al., 2017; Song et al., 2017; nephelinite: Cheng et al., 2015; lamprophyres: Wang, 2014; syenite: Zou et al., 2015; basalts: Tian et al., 2010; Xu et al., 2014; picrite: Tian et al., 2010; Tarim basements: Zhang et al., 2008.

the carbonatites and alkaline rocks may derive from the same lithospheric mantle source, different from the deep-seated plume. A mantle plume may provide sufficient thermal energy to produce a low-degree partial melting of carbonated peridotites. Therefore, the wide emplacement of carbonatites and alkaline complexes before and at the end of flood basalt eruption is unrelated to the plume compositions but may be to the thermal energy contribution.

The petrogenesis of carbonatitic parental magmas remains unclear. Three models have been used to demonstrate experimental and geochemical data in the past several decades (e.g., Yaxley et al., 2022): (1) formed directly by low-degree partial melting of a carbonated mantle (e.g., Dalton and Presnall, 1998; Yaxley and Brey, 2004), (2) residual melts of extreme fractional crystallization of a carbonated silica-undersaturated silicate magma (e.g., Lee and Wyllie, 1997; Veksler et al., 1998), and (3) liquid immiscibility from carbonated silicate magmas (e.g., Brooker and Kjarsgaard, 2011; Berndt and Klemme, 2022). Based on the field relationship, the dolomite carbonatite crystallized earlier than calcite carbonatite (Cheng et al., 2018). The fractional crystallization and liquid immiscibility of carbonated silicate melts cannot explain the carbonatite origins. Both Bachu dolomite and calcite carbonatites formed at ca. 300 Ma (Fig. 8) and are older than the associated alkalic rocks of nephelinite, lamprophyre, and syenite (ca. 270–275 Ma; Wang, 2014; Cheng et al., 2015; Zou et al., 2015). Experimental and melt inclusion data suggest that carbonatite melts formed by liquid immiscibility from a silica-undersaturated alkaline silicate magma are moderately alkaline, with Ca-rich carbonatite composition with significant amounts of SiO_2 + Al_2O_3 (~10 wt%; Brooker and Kjarsgaard, 2011; Berndt and Klemme, 2022), in contrast to the early silicate-poor, dolomite carbonatites. Moreover, carbonatite melt origin via fractional crystallization of alkaline silicate magmas is characterized by high-alkali and Ca-rich compositions and strong HFSE enrichment with the occurrence of pyrochlore and baddeleyite (Veksler et al., 1998). This result is not observed in the carbonatite samples. Therefore, the Bachu carbonatites may be formed by direct low-degree partial melting of the lithospheric mantle source.

5.2. HREE enrichment during magma evolution

Late magmatic-hydrothermal fluids can extract REE from magmatic REE-rich phases and re-distribute them to form new hydrothermal REE minerals. The magmatic process is a prerequisite to developing economic REE concentration in peralkaline granites and carbonatites (Gysi and Williams-Jones, 2013; Wei et al., 2022). Therefore, a fundamental understanding of the initial enrichment of HREE during magma evolution is crucial to understanding HREE mineralization. Magmatic processes related to REE enrichment in carbonatites include direct low-degree partial melting, immiscibility from silicate magmas, and fractional crystallization. Experimental data suggested that low-degree partial melting of carbonated peridotite or eclogite will produce LREE-rich carbonatitic melts with HREE depletion (e.g., Sweeney, 1994; Foley et al., 2009), consistent with melt inclusion observations (Guzmics et al. 2008; Walter et al., 2008). The REE distribution coefficients between immiscible carbonate–silicate melt have been experimentally demonstrated previously but show controversial behavior from different studies. In Veksler et al.'s (1998, 2012) work, REE, particularly HREE, has enriched in silicate melt rather than coexisting carbonate melt with a minor presence of P, F, and Cl. Subsequent experiments by Martin et al. (2013) and Nabyl et al. (2020) have shown that REE becomes compatible with carbonate melt in an H_2O-alkalis-bearing system, and the degree of REE enrichment in carbonate melt depends on the degree of differentiation of the associated alkaline rocks. These experiments have suggested that LREE has higher partition coefficients than HREE, and immiscibility may not be crucial for HREE enrichment in carbonatites. Many carbonatites formed by immiscible processes do not contain economic REE resources (e.g., Halama et al., 2004; Guzmics et al. 2011). The low viscosity of carbonatitic melts facilitates crystal fractionation during melt evolution (Kono et al., 2014). Crystal fractionation of dense silicates (i.e., pyroxene and mica) and sulfides from magmas cannot significantly affect the REE composition due to their minor modal abundance and relatively low REE concentrations (Reguir et al., 2012). The oxides such as pyrochlore and perovskite in carbonatites are usually LREE-dominated (Hornig-Kjarsgaard, 1998), and their early fractionation will reduce the LREE contents of the residual melt. However, fractional crystallization of carbonate minerals may lead to REE enrichment in the evolved carbonatite magmas (Cheng et al., 2018).

Our geochemical data reveal that the HREE contents increase remarkably from the dolomite to calcite carbonatites. Variable HREE composition was determined in their mineral phases. In calcite carbonatites, the rock-forming calcite contains higher HREE concentrations and is characterized by lower La/Ybcn (~0.3) ratios than the magmatic dolomite with a strong LREE enrichment. Their apatite exhibits different LREE patterns, but Types C1, C2, and C3 have a consistently higher amounts of HREE (Y_2O_3 up to 2 wt%) than those in the dolomite rocks (most Y_2O_3 below the EPMA detection limit) (Fig. 4B, 5B). Differences in REE concentrations of apatites are probably due to the compositions of carbonatitic melts or fluids from which they precipitate (Nathwani et al., 2020). A similar difference in HREE content was observed in the LREE minerals of monazite, bastnäsite, and parisite from the dolomite and calcite carbonatites. The latter contains significantly higher HREE (Figs. 5C, 7). Xenotime is only present in the calcite carbonatite.

The corresponding change in LREE to HREE enrichment in the transition from the dolomite to calcite carbonatites suggests that REE fractionation may be related to the extensive fractionation of rock-forming carbonate minerals. The REE patterns of primary mineral phases (i.e., dolomite and apatite) in the dolomite carbonatite show a steep negative slope with a strong LREE enrichment (Fig. 5A, B). This finding indicates that during the crystallization of dolomite carbonatite, HREE are incompatible with the early-crystallization dolomite and apatite and are therefore retained in the residual melt. Dolomites are principal constituents of the rocks (volume up to 90%). Moreover, field observation shows that the exposed scale of dolomite carbonatites is larger than that of calcite carbonatite, which indicates that dolomite imposes significant control on REE fractionation at the early stages of crystallization of carbonatitic magmas. The REE patterns of calcite from calcite carbonatites are nearly flat with HREE enrichment (Fig. 5A). Qualitative assessments of mineral and whole-rock geochemistry reveal that the partition coefficients of REE between calcite and carbonatite melts are low and gradually increase from La to Lu, indicating that HREE are more compatible with this mineral than LREE (Bühn, 2001; Dawson

and Hinton, 2003; Xu et al., 2010). Experiments conducted at high temperature and pressure conditions by Chebotarev et al. (2019) also support the results. Therefore, we infer that HREE have been incorporated into calcites with their progressive crystallization during the magmatic stage, forming nearly flat REE patterns.

5.3. HREE transportation and precipitation

Most REE deposits contain abundant fluorite, which is widely used as REE exploration indicator (Williams-Jones et al., 2000; Xu et al., 2012). Strzelecki et al. (2022) suggested that fluoride minerals (i.e., fluocerite) can serve as a precursor phase that fractionates LREE and HREE because the solubility of LREE fluorides is several orders of magnitude lower than that of HREE fluorides; thus, HREE are more mobile in hydrothermal systems. However, fluorite has not been observed in the Bachu deposit. Many xenotimes are closely associated with burbankite (Fig. 2A–D). The latter is considered a magmatic REE mineral and crystallizes directly from a carbonatite melt with highly concentrated alkalis (Chakhmouradian and Dahlgren, 2021; Nikolenko et al., 2022). However, it is rarely preserved in carbonatites and prone to alteration by post-magmatic hydrothermal fluids, resulting in the formation of hexagonal-like pseudomorphs consisting of insoluble residues of Ba–Sr–sulfates, strontianite, monazite, and REE–fluorocarbonate (Zaitsev et al., 2002; Chakhmouradian and Dahlgren, 2021). In the calcite carbonatites, most REE–Na-rich burbankites are preserved well in the structure and less affected by late fluid-induced alteration. It is well accepted that the carbonatitic magmas are initially alkali-rich, but they lost Na and K by exsolving the alkalis-bearing fluids to react with the wall rocks, forming fenite (Elliott et al., 2018). In Bachu, the well-preserved burbankite and limited fenitization indicate that the rocks retain sufficient alkalis during emplacement. Melt inclusion (Guzmics et al., 2011; Chayka et al., 2021), and experimental (Weidendorfer et al., 2017) studies demonstrated the alkalis would be enriched by fractional crystallization of a carbonatite magma, similar to the Bachu carbonatites.

Xenotime was observed to intergrow with alkali-rich aegirine, albite, and sulfate minerals (i.e., baryte, celestine), and quartz in many cases (Fig. 2). The REE are generally considered to be transported as chloride and sulfate complexes in hydrothermal systems, and the latter may be the main HREE transport ligand due to the non-selective mobilization of REE (Migdisov et al., 2016). Anenburg et al. (2020) experimentally demonstrated that the alkalis may substantially enhance REE solubility and produce high HREE/LREE ratios in a carbonatitic magmatic-hydrothermal system. This conclusion is further supported by natural evidence showing that alkali-rich fenites display higher HREE concentrations than the associated carbonatite intrusions (Elliott et al., 2018; Broom-Fendley et al., 2021). In addition, experimental studies and simulated calculations have shown that the solubility of Si in carbonatite magmas is low, and many silicates, especially quartz in carbonatites, may be scavenged from the wall-rocks via melt-rock reaction (Weidendorfer and Asimow, 2022; Anenburg and Guzmics, 2023). The input of silicates facilitates precipitation of the HREE minerals from the REE-alkali complexes due to the formation of alkali-rich silicate minerals such as aegirine and albite (Anenburg et al., 2020). In addition, silicon promotes the incorporation of REE into apatite in carbonatite systems, particularly HREE (e.g., $D^{La}_{apatite/melt}$ = 1.36–1.43, $D^{Yb}_{apatite/melt}$ = 2.96–3.06; Hammouda et al., 2010). In contrast, all REE are incompatible with apatite in silica-poor systems ($D^{apatite/melt}_{REE} < 1$, Klemme and Dalpé, 2003). This condition is consistent with our result (Fig. 6), showing that Y positively correlates with Si concentrations in the apatites. Therefore, alkalis may enhance REE, particularly HREE migration in evolved carbonatite melts, and Si assimilation may lead to Na-K deposition and HREE mineralization in the carbonatites.

6. Conclusions

The Bachu REE deposit is hosted by dolomite and calcite carbonatites, which were formed before the major eruption epoch of the Tarim flood basalts and show entirely different Sr-Nd isotopic compositions to the basalts. The carbonatites were derived directly from the low-degree melting of lithospheric mantle sources induced by thermal perturbation from a deep-seated mantle plume. The calcite carbonatites crystallized later than the dolomite rocks. They show remarkably enriched evolution of HREE from the dolomite to calcite carbonatites, as evidenced by HREE-bearing carbonates, apatite, monazite, REE-fluorcarbonates, and characteristic xenotime in the calcite carbonatite. Based on the magma evolution sequence and detailed mineralogy and geochemistry, we infer that the crystallization of LREE- and Mg-rich dolomite carbonatites caused the residual carbonate melts to become relatively enriched in Ca, alkalis, and REE. Moreover, alkalis promoted REE, particularly HREE transportation and enrichment, and input of the Si from the wall rocks destabilised the REE-alkali complex to form LREE and HREE minerals. Therefore, strong fractional crystallization and alkali preservation may potentially contribute to HREE mineralization in carbonatites.

Declaration of Competing Interest

The authors declare that they have no known competing financial interests or personal relationships that could have appeared to influence the work reported in this paper.

Acknowledgments

This research was financially supported by the National Natural Science Foundation of China (92162219, 41973036, 42273070, and 42202102) and the Guangxi Key Research and Development Project (Guike AB22035045). MS acknowledges support from the UK-RI Natural Environment Research Council grant NE/V008935/1. J.K. was supported by the Czech Science Foundation GACR EXPRO (grant number 19-29124X). We are grateful to Editors Jeffrey G. Catalano, Adam Simon, and Franco Pirajno, Michael Anenburg and one anonymous reviewer for their constructive comments.

Appendix A. Supplementary material

The supplementary document associated with this paper contains four figures and six tables. The supplementary figures are provided as a PDF file and the analyzed data are provided as an Excel file. Supplementary material to this article can be found online at https://doi.org/10.1016/j.gca.2023.08.025.

References

Anenburg, M., Guzmics, T., 2023. Silica is unlikely to be soluble in upper crustal carbonatite melts. Nat. Commun. 14, 942.

Anenburg, M., Mavrogenes, J.A., Frigo, C., Wall, F., 2020. Rare earth element mobility in and around carbonatites controlled by sodium, potassium, and silica. Sci. Adv. 6, eabb6570.

Bell, K., Tilton, G.R., 2001. Nd, Pb and Sr isotopic compositions of East African carbonatites: Evidence for mantle mixing and plume inhomogeneity. J. Petrol. 42, 1927–1945.

Berndt, J., Klemme, S., 2022. Origin of carbonatites-liquid immiscibility caught in the act. Nat. Commun. 13, 2892.

Bodeving, S., Williams-Jones, A.E., Swinden, S., 2017. Carbonate–silicate melt immiscibility, REE mineralising fluids, and the evolution of the Lofdal intrusive suite, Namibia. Lithos 268, 383–398.

Brooker, R.A., Kjarsgaard, B.A., 2011. Silicate–carbonate liquid immiscibility and phase relations in the system SiO_2-Na_2O-Al_2O_3-CaO-CO_2 at 0.1-2.5 GPa with applications to carbonatite genesis. J. Petrol. 52, 1281–1305.

Broom-Fendley, S., Brady, A.E., Wall, F., Gunn, G., Dawes, W., 2017. REE minerals at the Songwe Hill carbonatite, Malawi: HREE-enrichment in late-stage apatite. Ore Geol. Rev. 81, 23–41.

Broom-Fendley, S., Elliott, H.A.L., Beard, C.D., Wall, F., Armitage, P.E.B., Brady, A.E., Deady, E., Dawes, W., 2021. Enrichment of heavy REE and Th in carbonatite-derived fenite breccia. Geol. Mag. 158, 2025–2041.

Bühn, B., 2001. Rare-earth element systematics of carbonatitic fluorapatites, and their significance for carbonatite magma evolution. Contrib. Miner. Petrol. 141, 572–591.

Chakhmouradian, A.R., Dahlgren, S., 2021. Primary inclusions of burbankite in carbonatites from the Fen complex, southern Norway. Mineral. Petrol. 115, 161–171.

Chayka, I.F., Kamenetsky, V.S., Vladykin, N.V., Kontonikas-Charos, A., Prokopyev, I.R., Stepanov, S.Y., Krasheninnikov, S.P., 2021. Origin of alkali-rich volcanic and alkali-poor intrusive carbonatites from a common parental magma. Sci. Rep. 11, 17627.

Chebotarev, D.A., Veksler, I.V., Wohlgemuth-Ueberwasser, C., Doroshkevich, A.G., Koch-Müller, M., 2019. Experimental study of trace element distribution between calcite, fluorite and carbonatitic melt in the system $CaCO_3 + CaF_2 + Na_2CO_3 \pm Ca_3(PO_4)_2$ at 100 MPa. Contrib. Miner. Petrol. 174, 1–13.

Cheng, Z.G., Zhang, Z.C., Hou, T., Santosh, M., Zhang, D.Y., Ke, S., 2015. Petrogenesis of nephelinites from the Tarim large igneous province, NW China: Implications for mantle source characteristics and plume–lithosphere interaction. Lithos 220, 164–178.

Cheng, Z.G., Zhang, Z.C., Hou, T., Santosh, M., Chen, L.L., Ke, S., Xu, L.J., 2017. Decoupling of Mg–C and Sr–Nd–O isotopes traces the role of recycled carbon in magnesiocarbonatites from the Tarim large igneous province. Geochim. Cosmochim. Acta 202, 159–178.

Cheng, Z.G., Zhang, Z.C., Aibai, A., Kong, W.L., Holtz, F., 2018. The role of magmatic and post-magmatic hydrothermal processes on rare-earth element mineralization: A study of the Bachu carbonatites from the Tarim large igneous province, NW China. Lithos 314, 71–87.

Dalton, J.A., Presnall, D.C., 1998. Carbonatitic melts along the solidus of model lherzolite in the system $CaO\text{-}MgO\text{-}Al_2O_3\text{-}SiO_2\text{-}CO_2$ from 3 to 7 GPa. Contrib. Miner. Petrol. 131, 123–135.

Dawson, J.B., Hinton, R.W., 2003. Trace-element content and partitioning in calcite, dolomite and apatite in carbonatite, Phalaborwa, South Africa. Mineral. Mag. 67, 921–930.

Elliott, H.A.L., Wall, F., Chakhmouradian, A.R., Siegfried, P.R., Dahlgren, S., Weatherley, S., Finch, A.A., Marks, M.A.W., Dowman, E., Deady, E., 2018. Fenites associated with carbonatite complexes: A review. Ore Geol. Rev. 93, 38–59.

Ernst, R.E., Bell, K., 2010. Large igneous provinces (LIPs) and carbonatites. Mineral. Petrol. 98, 55–76.

Fischer, T.P., Burnard, P., Marty, B., Hilton, D.R., Furi, E., Palhol, F., Sharp, Z.D., Mangasini, F., 2009. Upper-mantle volatile chemistry at Oldoinyo Lengai volcano and the origin of carbonatites. Nature 459, 77–80.

Foley, S.F., Yaxley, G.M., Rosenthal, A., Buhre, S., Kiseeva, E.S., Rapp, R.P., Jacob, D.E., 2009. The composition of near-solidus melts of peridotite in the presence of CO_2 and H_2O between 40 and 60 kbar. Lithos 112, 274–283.

Goodenough, K.M., Wall, F., Merriman, D., 2017. The rare earth elements: Demand, global resources, and challenges for resourcing future generations. Nat. Resour. Res. 27, 201–216.

Guzmics, T., Zajacz, Z., Kodolányi, J., Halter, W., Szabó, C., 2008. LA-ICP-MS study of apatite- and K feldspar-hosted primary carbonatite melt inclusions in clinopyroxenite xenoliths from lamprophyres, Hungary: Implications for significance of carbonatite melts in the Earth's mantle. Geochim. Cosmochim. Acta 72, 1864–1886.

Guzmics, T., Mitchell, R.H., Szabó, C., Márta, B., Milke, R., Abart, R., 2011. Carbonatite melt inclusions in coexisting magnetite, apatite and monticellite in Kerimasi calciocarbonatite, Tanzania: Melt evolution and petrogenesis. Contrib. Miner. Petrol. 161, 177–196.

Gysi, A.P., Williams-Jones, A.E., 2013. Hydrothermal mobilization of pegmatite-hosted REE and Zr at Strange Lake, Canada: A reaction path model. Geochim. Cosmochim. Acta 122, 324–352.

Halama, R., Venneman, T., Siebel, W., Marka, G., 2004. The Gronnedal-Ika carbonatite-syenite complex, South Greenland: Carbonatite formation by liquid immiscibility. J. Petrol. 46, 191–217.

Hammouda, T., Chantel, J., Devidal, J.L., 2010. Apatite solubility in carbonatitic liquids and trace element partitioning between apatite and carbonatite at high pressure. Geochim. Cosmochim. Acta 74, 7220–7235.

Hornig-Kjarsgaard, I., 1998. Rare earth elements in sovitic carbonatites and their mineral phases. J. Petrol. 39, 2105–2121.

Humphreys-Williams, E.R., Zahirovic, S., 2021. Carbonatites and global tectonics. Elements 17, 339–344.

Klemme, S., Dalpé, C., 2003. Trace-element partitioning between apatite and carbonatite melt. Am. Mineral. 88, 639–646.

Kono, Y., Kenney-Benson, C., Hummer, D., Ohfuji, H., Park, C., Shen, G., Wang, Y., Kavner, A., Manning, C.E., 2014. Ultralow viscosity of carbonate melts at high pressures. Nat. Commun. 5, 5091.

Lee, W.J., Wyllie, P.J., 1997. Liquid immiscibility between nephelinite and carbonatite from 1.0 to 2.5 GPa compared with mantle melt compositions. Contrib. Miner. Petrol. 127, 1–16.

Louvel, M., Etschmann, B., Guan, Q., Testemale, D., Brugger, J., 2022. Carbonate complexation enhances hydrothermal transport of rare earth elements in alkaline fluids. Nat. Commun. 13, 1456.

Martin, L.H.J., Schmidt, M.W., Mattsson, H.B., Guenther, D., 2013. Element partitioning between immiscible carbonatite and silicate melts for dry and H2O-bearing systems at 1–3 GPa. J. Petrol. 54, 2301–2338.

Migdisov, A., Williams-Jones, A.E., Brugger, J., Caporuscio, F.A., 2016. Hydrothermal transport, deposition, and fractionation of the REE: Experimental data and thermodynamic calculations. Chem. Geol. 439, 13–42.

Mollé, V., Gaillard, F., Nabyl, Z., Tuduri, J., Di Carlo, I., Erdmann, S., 2021. Crystallisation sequence of a REE-rich carbonate melt: An experimental approach. Comptes Rendus. Géoscience 353, 217–231.

Nabyl, Z., Massuyeau, M., Gaillard, F., Tuduri, J., Iacono-Marziano, G., Rogerie, G., Le Trong, E., Di Carlo, I., Melleton, J., Bailly, L., 2020. A window in the course of alkaline magma differentiation conducive to immiscible REE-rich carbonatites. Geochim. Cosmochim. Acta 282, 297–323.

Nathwani, C.L., Loader, M.A., Wilkinson, J.J., Buret, Y., Sievwright, R.H., Hollings, P., 2020. Multi-stage arc magma evolution recorded by apatite in volcanic rocks. Geology 48, 323–327.

Nikolenko, A.M., Stepanov, K.M., Roddatis, V., Veksler, I.V., 2022. Crystallization of bastnäsite and burbankite from carbonatite melt in the system $La(CO_3)F\text{-}CaCO_3\text{-}Na_2CO_3$ at 100 MPa. Amer. Mineral. 107, 2242–2250.

Pouchou, J.L., Pichoir, F., 1984. A new model for quantitative X-ray microanalysis. Part I: Application to the analysis of homogeneous samples. Rech. Aerospat. 167–192.

Reguir, E.P., Chakhmouradian, A.R., Pisiak, L., Halden, N.M., Yang, P., Xu, C., Kynický, J., Couëslan, C.G., 2012. Trace-element composition and zoning in clinopyroxene- and amphibole-group minerals: Implications for element partitioning and evolution of carbonatites. Lithos 128–131, 27–45.

Simonetti, A., Goldstein, S.L., Schmidberger, S.S., Viladkar, S.G., 1998. Geochemical and Nd, Pb, and Sr isotope data from Deccan alkaline complexes–inferences for mantle sources and plume-lithosphere interaction. J. Petrol. 39, 1847–1864.

Smith, M., Kynicky, J., Xu, C., Song, W., Spratt, J., Jeffries, T., Brtnicky, M., Kopriva, A., Cangelosi, D., 2018. The origin of secondary heavy rare earth element enrichment in carbonatites: Constraints from the evolution of the Huanglongpu district, China. Lithos 308, 65–82.

Song, W.L., Xu, C., Smith, M.P., Kynicky, J., Huang, K., Wei, C.W., Zhou, L., Shu, Q.H., 2016. Origin of unusual HREE-Mo-rich carbonatites in the Qinling Orogen, China. Sci. Rep. 6, 37377.

Song, W.L., Xu, C., Chakhmouradian, A.R., Kynicky, J., Huang, K., Zhang, Z., 2017. Carbonatites of Tarim (NW China): First evidence of crustal contribution in carbonatites from a large igneous province. Lithos 282–283, 1–9.

Song, W.L., Xu, C., Smith, M.P., Chakhmouradian, A.R., Brenna, M., Kynicky, J., Chen, W., Yang, Y.H., Deng, M., Tang, H.Y., 2018. Genesis of the world's largest rare earth element deposit, Bayan Obo, China: Protracted mineralization evolution over ~1 b.y. Geology 46, 323–326.

Strzelecki, A.C., Migdisov, A., Boukhalfa, H., Sauer, K., McIntosh, K.G., Currier, R.P., Williams-Jones, A.E., Guo, X., 2022. Fluocerite as a precursor to rare earth element fractionation in ore-forming systems. Nat. Geosci. 15, 327–333.

Sweeney, R.J., 1994. Carbonatite melt compositions in the Earth's mantle. Earth Planet. Sci. Lett. 128, 259–270.

Tian, W., Campbell, I.H., Allen, C.M., Guan, P., Pan, W.Q., Chen, M.M., Yu, H.J., Zhu, W. P., 2010. The Tarim picrite–basalt–rhyolite suite, a Permian flood basalt from northwest China with contrasting rhyolites produced by fractional crystallization and anatexis. Contrib. Miner. Petrol. 160, 407–425.

Tong, X., Liu, Y., Hu, Z., Chen, H., Zhou, L., Hu, Q., Xu, R., Deng, L., Chen, C., Yang, L., Gao, S., 2015. Accurate determination of Sr isotopic compositions in clinopyroxene and silicate glasses by LA-MC-ICP-MS. Geostand. Geoanal. Res. 40, 85–99.

Veksler, I.V., Petibon, C., Jenner, G.A., Dorfman, A.M., Dingwell, D.B., 1998. Trace element partitioning in immiscible silicate-carbonate liquid systems: An initial experimental study using a centrifuge autoclave. J. Petrol. 39, 2095–2104.

Veksler, I.V., Dorfman, A.M., Dulski, P., Kamenetsky, V.S., Danyushevsky, L.V., Jeffries, T., Dingwell, D.B., 2012. Partitioning of elements between silicate melt and immiscible fluoride, chloride, carbonate, phosphate and sulfate melts, with implications to the origin of natrocarbonatite. Geochim. Cosmochim. Acta 79, 20–40.

Wall, F., Niku-Paavola, V.N., Storey, C., Muller, A., Jeffries, T., 2008. Xenotime-(Y) from carbonatite dykes at Lofdal, Namibia: Unusually low LREE:HREE ratio in carbonatite, and the first dating of xenotime overgrowths on zircon. Can. Mineral. 46, 861–877.

Wall, F., Rollat, A., Pell, R.S., 2017. Responsible sourcing of critical metals. Elements 13, 313–318.

Walter, M.J., Bulanova, G.P., Armstrong, L.S., Keshav, S., Blundy, J.D., Gudfinnsson, G., Lord, O.T., Lennie, A.R., Clark, S.M., Smith, C.B., Gobbo, L., 2008. Primary carbonatite melt from deeply subducted oceanic crust. Nature 454, 622–625.

Wang, L., 2014. The mineralogy, geochemistry and source region of agpaitic lamprophyre in Wajilitage, XinJiang. A dissertation of Master Degree for China. University of Geosciences, Beijing, China.

Watts, K.E., Haxel, G.B., Miller, D.M., 2022. Temporal and petrogenetic links between Mesoproterozoic alkaline and carbonatite magmas at Mountain Pass, California. Econ. Geol. 117, 1–23.

Wei, C.W., Deng, M., Xu, C., Chakhmouradian, A.R., Smith, M.P., Kynicky, J., Song, W.L., Chen, W., Fu, B., 2022. Mineralization of the Bayan Obo rare earth element deposit by recrystallization and decarbonation. Econ. Geol. 117, 1327–1338.

Weidendorfer, D., Asimow, P.D., 2022. Experimental constraints on truly conjugate alkaline silicate–carbonatite melt pairs. Earth Planet. Sci. Lett. 584, 117500.

Weidendorfer, D., Schmidt, M.W., Mattsson, H.B., 2017. A common origin of carbonatite magmas. Geology 45, 507–510.

Williams-Jones, A.E., Samson, I.M., Olivo, G.R., 2000. The genesis of hydrothermal fluorite-REE deposits in the Gallinas Mountains, New Mexico. Econ. Geol. 95, 327–341.

Woolley, A.R., Bailey, D.K., 2012. The crucial role of lithospheric structure in the generation and release of carbonatites: Geological evidence. Mineral. Mag. 76, 259–270.

Woolley, A.R., Kempe, D.R.C., 1989. Carbonatites: Nomenclature, average chemical compositions, and element distribution. In: Bell, K. (Ed.), Carbonatites, Genesis and Evolution, London UK, pp. 1–14.

Xu, C., Kynicky, J., Chakhmouradian, A.R., Campbell, I.H., Allen, C.M., 2010. Trace-element modeling of the magmatic evolution of rare-earth-rich carbonatite from the Miaoya deposit, Central China. Lithos 118, 145–155.

Xu, C., Taylor, R.N., Li, W., Kynicky, J., Chakhmouradian, A.R., Song, W.L., 2012. Comparison of fluorite geochemistry from REE deposits in the Panxi region and Bayan Obo, China. J. Asian Earth Sci. 57, 76–89.

Xu, C., Kynicky, J., Smith, M.P., Kopriva, A., Brtnicky, M., Urubek, T., Yang, Y., Zhao, Z., He, C., Song, W., 2017. Origin of heavy rare earth mineralization in South China. Nat. Commun. 8, 14598.

Xu, Y.G., Wei, X., Luo, Z.Y., Liu, H.Q., Cao, J., 2014. The Early Permian Tarim large igneous province: Main characteristics and a plume incubation model. Lithos 204, 20–35.

Yang, Y.H., Sun, J., Xie, L.W., Fan, H.R., Wu, F.Y., 2008. In situ Nd isotopic measurement of natural geological materials by LA-MC-ICPMS. Sci. Bull. 53, 1062–1070.

Yaxley, G.M., Brey, G.P., 2004. Phase relations of carbonate-bearing eclogite assemblages from 2.5 to 5.5 GPa: Implications for petrogenesis of carbonatites. Contrib. Miner. Petrol. 146, 606–619.

Yaxley, G.M., Anenburg, M., Tappe, S., Decree, S., Guzmics, T., 2022. Carbonatites: Classification, sources, evolution, and emplacement. Ann. Rev. Earth Planet. Sci. 50, 261–293.

Zaitsev, A.N., Demény, A., Sindern, S., Wall, F., 2002. Burbankite group minerals and their alteration in rare earth carbonatites—source of elements and fluids (evidence from C-O and Sr–Nd isotopic data). Lithos 62, 15–33.

Zhang, C.L., Li, X.H., Li, Z.X., Ye, H.M., Li, C.N., 2008. A Permian layered intrusive complex in the western Tarim Block, Northwestern China: Product of a Ca. 275-Ma Mantle Plume? J. Geol. 116, 269–287.

Zhang, D.Y., Zhang, Z.C., Santosh, M., Cheng, Z., He, H., Kang, J.L., 2013. Perovskite and baddeleyite from kimberlitic intrusions in the Tarim large igneous province signal the onset of an end-Carboniferous mantle plume. Earth Planet. Sci. Lett. 361, 238–248.

Zou, S.Y., Li, Z.L., Song, B., Ernst, R.E., Li, Y.Q., Ren, Z.Y., Yang, S.F., Chen, H.L., Xu, Y. G., Song, X.Y., 2015. Zircon U-Pb dating, geochemistry and Sr–Nd–Pb–Hf isotopes of the Wajilitag alkali mafic dikes, and associated diorite and syenitic rocks: Implications for magmatic evolution of the Tarim large igneous province. Lithos 212, 428–442.